INORGANIC CHEMISTRY FRONTIERS

RESEARCH ARTICLE

View Article Online
View Journal | View Issue

Check for updates

Cite this: *Inorg. Chem. Front.*, 2021, **8**, 1695

# Efficient and steady production of 1 : 2 syngas ($CO/H_2$) by simultaneous electrochemical reduction of $CO_2$ and $H_2O$†

Wei Yang,‡[a] Ji-Hong Zhang,‡[a] Rui Si,[b] Li-Ming Cao,[a] Di-Chang Zhong *[a] and Tong-Bu Lu[a]

Received 17th November 2020,
Accepted 5th January 2021

DOI: 10.1039/d0qi01351j

rsc.li/frontiers-inorganic

Efficient generation of synthetic gas (syngas) through the electrochemical reduction of $CO_2$ and $H_2O$ is a promising route to realize the conversion and storage of electricity. The production of syngas with a controlled $CO/H_2$ ratio is significant for the subsequent preparation of value-added chemicals. Herein, a guest–host pyrolysis strategy is employed to synthesize Co–$C/N_x$-based single-site catalytic materials. The as-prepared materials possess a high graphitic degree of carbon, which supports the rapid electron transport and promotes efficient electrochemical reduction reactions. As a result, these materials can serve as excellent electrocatalysts for the production of syngas by the electrochemical reduction of $CO_2$ and $H_2O$, which exhibits high production rates and steady $CO/H_2$ ratio (v : v = 1 : 2) at wide-range electrochemical windows. The faradaic efficiency reaches nearly 100%, and the formation rate reaches as high as 1.08 mol $g^{-1}$ $h^{-1}$ at 1.0 V *vs.* RHE.

Published on 06 2021. Downloaded on 24.01.26 11:12:02.

## 1. Introduction

Synthetic gas (syngas), a mixture of carbon monoxide (CO) and hydrogen ($H_2$), is one of the most important types of raw materials for producing synthetic fuels and value-added industrial chemicals.[1–6] Owing to the increase in the energy consumption and environmental concerns induced by the excessive usage of fossil fuels, syngas may become an important alternative carbon resource replacing fossil fuels. Conventionally, syngas is generated by reforming non-renewable fossil fuels under a high temperature.[7,8] The pathway requires substantial separation and refinement operation steps, which increase the consumption of fossil fuel and aggravate the energy crisis. The electrochemical reduction of $CO_2$ and $H_2O$ is a promising route to produce syngas because of its high energy-conversion efficiency and production rates.[9–14] The key to this technology was to develop suitable electrocatalysts that could finely balance the $CO_2$ reduction reaction ($CO_2$RR) and the hydrogen evolution reaction (HER) to precisely control the $CO/H_2$ ratios. Several electrocatalysts with high catalytic activities for syngas production have been reported. For example, Kang *et al.* built a three-component catalytic system by combining $Co_3O_4$, CDots and $C_3N_4$, with which the $CO/H_2$ ratio could be tuned from 1 : 4 to 1 : 0.07 by controlling the applied potential.[15] Zeng *et al.* developed a series of $CdS_xSe_{1-x}$ catalysts for the production of syngas. They observed that with an increase in Se content in $CdS_xSe_{1-x}$, the FE for $H_2$ production increased. At −1.2 V *vs.* RHE, the ratio of $CO/H_2$ in the products varied from 4 : 1 to 1 : 4 in $CdS_xSe_{1-x}$ nanorods ($x$ is from 1 to 0).[16] We found that a Ni(II) tripodal complex could be utilized as an electrocatalyst for the production of syngas in a water-containing medium. The composition of the evolved syngas could be well tuned by varying the applied potential.[17]

In mature syngas conversion technologies, the syngas used for the synthesis of downstream products was usually in certain ratios of $CO/H_2$. For instance, a ratio of $CO/H_2$ of 1 : 0.6 was often used to produce hydrocarbons by Fischer–Tropsch process,[18–22] and a ratio of $CO/H_2$ of 1 : 2 was often used for methanol production.[23] Therefore, an efficient production of syngas with a desired $CO/H_2$ ratio was significant and much in demand. In this case, the syngas could be directly used, and no purification cost was involved. Among the downstream products of syngas, methanol is an important substance in the current chemical industry. Thus, a controlled synthesis of syngas with a 1 : 2 ratio of $CO/H_2$ is much desired. Although several electrocatalysts can produce syngas with a 1 : 2 ratio of

[a]*Institute for New Energy Materials and Low Carbon Technologies, School of Materials Science and Engineering, Tianjin University of Technology, Tianjin 300384, China. E-mail: dczhong@email.tjut.edu.cn*
[b]*Shanghai Synchrotron Radiation Facility, Shanghai Institute of Applied Physics, Chinese Academy of Sciences, Shanghai 201204, China*

†Electronic supplementary information (ESI) available: Experimental section and supplementary figures. See DOI: 10.1039/D0QI01351J

‡These authors contributed equally to this work.

Published on 06 2021. Downloaded on 24.01.26 11:12:02.

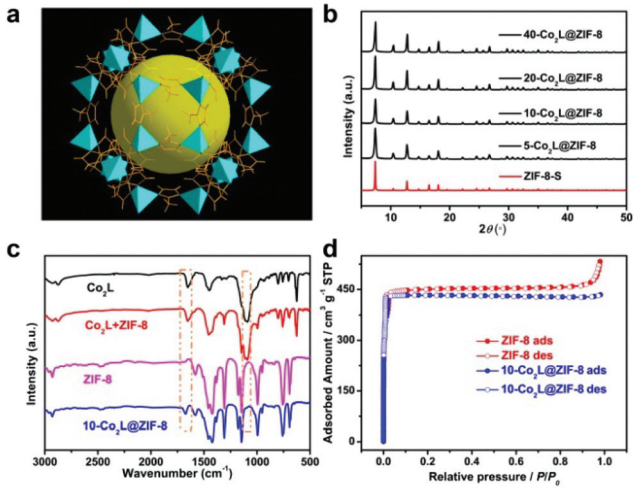


**Fig. 1** (a) Cage structure of $Co_2L$@ZIF-8. (b) PXRD patterns of *x*-$Co_2L$@ZIF-8. (c) FT-IR spectra of $Co_2L$, ZIF-8, physically mixed $Co_2L$ + ZIF-8, and host–guest $Co_2L$@ZIF-8. (d) $N_2$ adsorption isotherms of ZIF-8 and 10-$Co_2L$@ZIF-8 at 77 K.

CO/$H_2$,[23,24] those with low onset overpotential, high current density, and wide electrochemical window are still highly desired.

Herein, we proposed a guest–host pyrolysis strategy[25–30] to prepare Co single-site catalysts for an efficient electrocatalytic reduction of $CO_2$ and $H_2O$ to steadily produce syngas with a 1 : 2 ratio of CO/$H_2$ at a wide electrochemical window. First, we encapsulated a dinuclear Co(II) cryptate molecular complex ($[Co_2(OH)L](ClO_4)_3$ ($Co_2L$; L = $N[(CH_2)_2NHCH_2(m\text{-}C_6H_4)CH_2NH(CH_2)_2]_3N$)[31,32] into a structurally caged ZIF-8 (Fig. 1a). The resultant $Co_2L$@ZIF-8 with different amounts of $Co_2L$ were pyrolyzed at different temperatures to obtain a series of Co–carbon/nitrogen (Co–C/N*x*)-based catalysts. As the cages in ZIF-8 could serve as molecular fences to spatially separate the $Co_2L$ precursors, the generated cobalt atoms would not aggregate during the pyrolysis process. Consequently, single-site Co–carbon/nitrogen (Co–C/$N_X$)-based catalysts were successfully prepared by a guest–host pyrolysis strategy. More importantly, the as-obtained Co–C/$N_X$ catalysts demonstrated excellent catalytic performances for the production of syngas by the simultaneous electrochemical reduction of $CO_2$ and $H_2O$. The optimal catalyst exhibited an exceptionally high production rate of 1.08 mol $g^{-1}$ $h^{-1}$ at 1.0 V *vs.* RHE. Moreover, the ratio of CO/$H_2$ could be maintained as 1 : 2 at a wide electrochemical window of −1.0 to −0.5 V.

# 2. Experimental

## 2.1. Materials

All of the chemicals and materials were commercially obtained and used without further purification. Nafion solution (5 wt%) was purchased from Alfa Aesar. All of the solutions used in the electrochemical experiments were prepared with Millipore water (18.2 MΩ). The purity of both argon and $CO_2$ was 99.999%. $Co_2L$[33] and ZIF-8[27] were synthesized according to the literature methods.

## 2.2. Preparation

**2.2.1. *x*-$Co_2L$@ZIF-8.** 25 mL methanol containing $Zn(NO_3)_2 \cdot 6H_2O$ (950 mg, 5 mmol) and 5 mL $CH_3CN$ containing *x* mg $Co_2L$ (*x* = 5, 10, 20 and 40 mg) were homogeneously mixed, and then the mixture was slowly added to 25 mL methanol solution containing 2-methylimidazole (2 g, 24.4 mmol). The obtained mixture was further stirred for 1 h and then maintained at room temperature for 24 h. *x*-$Co_2L$@ZIF-8 composites with different contents of $Co_2L$ were obtained as precipitates. They were centrifuged and washed with DMF and MeOH 3 times, respectively, and dried at 70 °C overnight (yield: *ca.* 850 mg).

**2.2.2. *x*-$Co_2L$@ZIF-8-*T*.** 100 mg *x*-$Co_2L$@ZIF-8 precursor prepared above was placed in a tube furnace and heated to a specified temperature (*T* = 650, 750, 850, and 950 °C) at a heating rate of 5 °C $min^{-1}$. After maintaining at this temperature for 2 h under a flow of Ar atmosphere, the furnace was cooled naturally to room temperature. *x*-$Co_2L$@ZIF-8-*T* with a yield of *ca.* 250 mg was obtained and used for the structural characterization and catalytic performance estimation. The contents of Co in *x*-$Co_2L$@ZIF-8-*T* were tested by ICP-MS, and the results are listed in Table S1.†

## 2.3. Characterization

Fourier transform infrared (FT-IR) spectra were recorded on a PerkinElmer Frontier Mid-IR FT-IR spectrometer in the 400–4000 $cm^{-1}$ region with KBr pellets. Powder X-ray diffraction (XRD) patterns were recorded on a Smart X-ray diffractometer (SmartLab 9 kW, Rigaku, Japan) equipped with graphite monochromatized with a Cu Kα source (radiation) ($\lambda$ = 1.54178 Å). Nitrogen sorption tests were performed on a multi-station specific surface micropore and vapor adsorption analyzer (BELSORP-Max, MicrotracBEL, Japan) at 77 K. X-ray photoelectron spectra (XPS) were measured on an ESCALAB 250 Xi. Scanning electron microscopy (SEM) images were recorded on a Verios 460 L Ultrahigh Resolution Scanning Electron Microscope. Transmission electron microscopy (TEM) measurements were carried out by using a Tecnai G2 Spirit TWIN at an acceleration voltage of 120 kV. HAADF-STEM images were obtained using a Transmission Electron Microscope with a probe corrector (Titan Themis Cubed G2 60-300, FEI). X-ray absorption fine structure (XAFS) spectra were obtained from BL14W1 beamline of Shanghai Synchrotron Radiation Facility (SSRF). The metal (Co and Zn) contents in the prepared catalysts were measured by inductively coupled plasma-atomic emission spectroscopy (ICP-AES, SPECTROBLUE). Raman spectra were acquired with a Horiba Jobin–Yvon LabRAM HR800 spectrometer using a 514.5 nm laser for excitation. Electrochemical measurements were carried out on a CHI 670E electrochemical workstation. The evolved CO and $H_2$ were monitored by using an Agilent 7820A gas chromatograph or a Shimadzu GC-2014 gas chro-

 This journal is © the Partner Organisations 2021

Published on 06 2021. Downloaded on 24.01.26 11:12:02.

matograph. The liquid product was characterized by $^1$H NMR on a Bruker AVANCE III HD using a pre-saturation sequence.

### 2.4. Electrochemical measurements

All of the electrochemical measurements were conducted in an airtight H-type cell using a CHI 670E electrochemical station with a three-electrode configuration. The H-type cell was separated by a Nafion membrane (Nafion 117, DuPont) and filled with 40 mL 0.1 M $KHCO_3$ aqueous solution in each side. A platinum foil and an Ag/AgCl (3 M KCl) electrode were used as the counter and reference electrodes, respectively. The working electrode was prepared as follows: 5 mg catalyst was dispersed in an ethanol solvent (1 mL) with 50 μL Nafion solution (5 wt% in water). The suspension was ultrasonicated for 30 min to generate a homogeneous ink. The ink was then drop-casted onto a piece of carbon cloth with a size of 0.5 cm × 2.0 cm with 0.5 mg cm$^{-2}$ loading for catalysts.

0.1 M $KHCO_3$ aqueous solution was used as the electrolyte (pH – 7.8). Prior to the tests, the electrolyte was purged with Ar or $CO_2$ for at least 20 min. The gas product was detected by gas chromatography (GC), and the liquid product was characterized by $^1$H NMR spectroscopy. The liquid product concentration was quantified by using dimethyl sulfoxide (DMSO) as the internal standard. Cyclic voltammetry (CV) measurements at 100 mV s$^{-1}$ were performed for 20 cycles prior to recording a linear scan voltammetry (LSV) at 10 mV s$^{-1}$ for each sample. Each sample on the same substrate was measured for at least three independent times. Electrochemical Impedance Spectroscopy (EIS) measurements were conducted in static solution at −1.2 V (*vs.* Ag/AgCl). The amplitude of the sinusoidal wave was 10 mV, and the frequency scan range was from 100 kHz to 100 Hz. EIS spectra were analyzed using the Nova software package. Unless otherwise stated, all experiments were performed at ambient temperature, and the electrode potentials were converted to the RHE scale using the equation $E$ (RHE) = $E$ (Ag/AgCl) + 0.197 V + 0.059 × pH. The mole number for a given gas product was calculated as below:

$$n_i = x_i \times \frac{Pv_0}{RT}$$

where $x_i$ is the volume fraction of the product by online GC, $v_0$ is the volume of airtight H-type cell by excluding 40 mL 0.1 M $KHCO_3$ electrolyte, $P$ = 101.3 kPa, $R$ is the gas constant, and $T$ is the room temperature (298.15 K).

The faradaic efficiencies (FE%) for CO and $H_2$ production were calculated at a given potential as follows:

$$FE\% = \frac{J_i}{J_{total}} \times 100\% = \frac{n_i \times N \times F}{\sum J_i} \times 100\%$$

where $J_i$ is the partial current density for product formation, $J_{total}$ is the total current density, $N$ is the number of electrons transferred for product formation, where $N$ is 2 for CO and $H_2$, $n_i$ is the production rate of CO or $H_2$ (measured by GC) and $F$ is the faradaic constant (96 485 C mol$^{-1}$).

## 3. Results and discussion

### 3.1. Structure and morphology

**3.1.1. *x*-$Co_2L$@ZIF-8.** The powder X-ray diffraction (PXRD) patterns demonstrated that the diffraction peaks of *x*-$Co_2L$@ZIF-8 completely matched with those obtained for ZIF-8, which indicated that the encapsulation of $Co_2L$ did not destroy the framework of ZIF-8 (Fig. 1b). Fourier transform infrared (FT-IR) spectroscopy showed that the characteristic absorbance peaks of 10-$Co_2L$@ZIF-8 were slightly different from the peaks of the physically mixed $Co_2L$ + ZIF-8, indicating the inherent interactions between $Co_2L$ and ZIF-8 in $Co_2L$@ZIF-8 (Fig. 1c). $N_2$ sorption measurements revealed that the Brunauer–Emmett–Teller (BET) surface area of 10-$Co_2L$@ZIF-8 (1583 m$^2$ g$^{-1}$) was slightly smaller in contrast to ZIF-8 (1824 m$^2$ g$^{-1}$), which illustrated that the encapsulation of $Co_2L$ occupied some pore volume of ZIF-8 and the successful encapsulation of $Co_2L$ by ZIF-8 (Fig. 1d).

**3.1.2. *x*-$Co_2L$@ZIF-8-*T*.** *x*-$Co_2L$@ZIF-8 composites were further pyrolyzed at different temperatures, affording a series of Co–C/N*x*-based catalysts (*x*-$Co_2L$@ZIF-8-*T*). For comparison, ZIF-8 was also pyrolyzed to form an N-doped nanoporous carbon (ZIF-8-*T*). Fig. 2a shows that the PXRD pattern of 10-$Co_2L$@ZIF-8-850 is similar to that of ZIF-8-850, and no extra diffraction peaks except broad diffraction peaks at ~25.3° corresponding to graphitic carbon were observed, indicating the absence of Co species aggregation. High resolution scanning electron microscopy (HRSEM) and transmission electron microscopy (TEM) measurements of the as-prepared 10-$Co_2L$@ZIF-8-850 exhibited an average diameter of ~100 nm and a regular polyhedral bulk morphology with a rugged surface (Fig. 2b–d), similar to that of ZIF-8-850 (Fig. S2†).

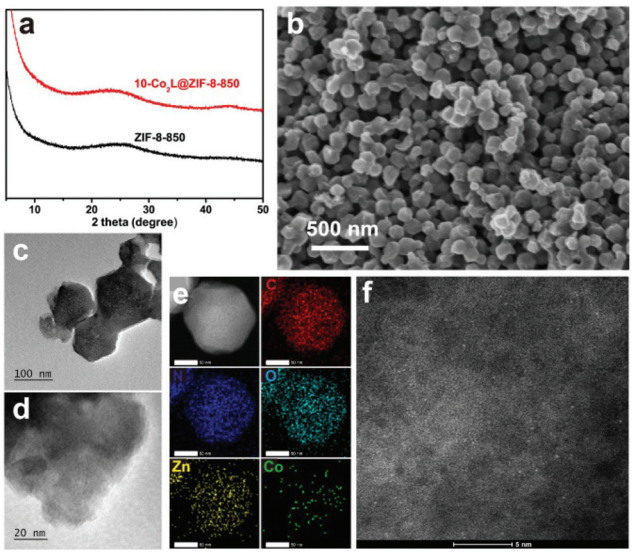


Fig. 2 (a) PXRD patterns of 10-$Co_2L$@ZIF-8 and ZIF-8-850. (b) SEM and (c, d) TEM images of 10-$Co_2L$@ZIF-8-850. (e) HRTEM images and the corresponding elemental mapping of 10-$Co_2L$@ZIF-8-850. (f) HAADF-STEM images of 10-$Co_2L$@ZIF-8-850.

Published on 06 2021. Downloaded on 24.01.26 11:12:02.

Consistent with the PXRD result, no Co species aggregation was observed in the TEM image (Fig. 2d), which indicated the presence of a single-site cobalt within 10-$Co_2$L@ZIF-8-850. The energy-dispersive X-ray spectroscopy (EDS) exhibited the uniform distributions of Zn, Co, C, and N, indicating that the Co atoms were highly-dispersed in 10-$Co_2$L@ZIF-8-850 (Fig. 2e). High-angle annular dark field STEM further demonstrated the single-site cobalt in 10-$Co_2$L@ZIF-8-850, where high density bright dots could be observed, which corresponded to the isolated Co atoms (Fig. 2f).

$N_2$ adsorption measurements were performed to evaluate the porosity of 10-$Co_2$L@ZIF-8-850 (Fig. S3†). The result showed that the Brunauer–Emmett–Teller (BET) surface area of 10-$Co_2$L@ZIF-8-850 is around 410 $m^2$ $g^{-1}$, which was significantly larger than those obtained for the carbon materials derived from the non-MOF based precursors,[34] thereby indicating that the porous precursors were useful to obtain the carbon materials with a high surface area and abundant porosity, which were conducive to the electrolyte diffusion and mass transfer in the electrocatalytic reactions.[35] Further gas sorption tests demonstrated that the large porosity of 10-$Co_2$L@ZIF-8-850 also endowed it with a remarkable $CO_2$ uptake capacity. As shown in Fig. S4,† at 298.15 K, the $CO_2$ capture capacity of $Co_2$L@ZIF-8-850 reaches as high as 53 $cm^3$ $g^{-1}$. The good $CO_2$ uptake might be ascribed to the suitable pore structure and the rich Co sites on the pore surface. Raman spectroscopy measurements were further carried out for 10-$Co_2$L@ZIF-8-850 and ZIF-8-850. As shown in Fig. S5,† the Raman spectrum of 10-$Co_2$L@ZIF-8-850 is similar to that of ZIF-8-850, with two peaks at 1335 and 1598 $cm^{-1}$, corresponding to the well-defined D band and G band, respectively. The ratio of the band intensity ($I_D/I_G$) for both the samples was approximately equal to 1 (Fig. S6†), which indicated a similar defect and graphitic degree of carbon in 10-$Co_2$L@ZIF-8-850 and ZIF-8-850.

XPS analyses were carried out to explore the elemental composition and the valence state in 10-$Co_2$L@ZIF-8-850 and ZIF-8-850. As shown in Fig. 3a and b, the survey spectrum only represents the elemental peaks of Zn, Co, C, N and O, consistent with the EDS analysis results (Fig. S1†). Two peaks at 796.6 and 781.1 eV as well as the two satellite peaks (Fig. 3c) could be attributed to Co $2p_{1/2}$ and Co $2p_{3/2}$, respectively. The broad peaks centered at 781.1 eV originated from the chemical bonding between Co and N, which confirmed the existence of Co–$N_x$ species in 10-$Co_2$L@ZIF-8-850. The broad and weak peaks might possibly be due to the very low Co contents.

The N atoms with different chemical states in both $Co_2$L@ZIF-8-850 and ZIF-8-850 could be demonstrated by deconvoluting N 1s signals. The five peaks at 398.3, 399.0, 400.2, 401.2 and 403.7 eV (Fig. S7b and S7e†) corresponded to the pyridinic N, Co–$N_x$, pyrrolic N, graphitic N, and oxide N, respectively.[36] The atomic contents of the pyridinic N, Co–$N_x$, pyrrolic N, graphitic N and N–O were determined to be 4.743, 2.981, 1.355, 1.704, 0.737% for 10-$Co_2$L@ZIF-8-850 and 4.757, 2.576, 0.846, 2.391 and 0.460% for ZIF-8-850, respectively (Fig. 3d).

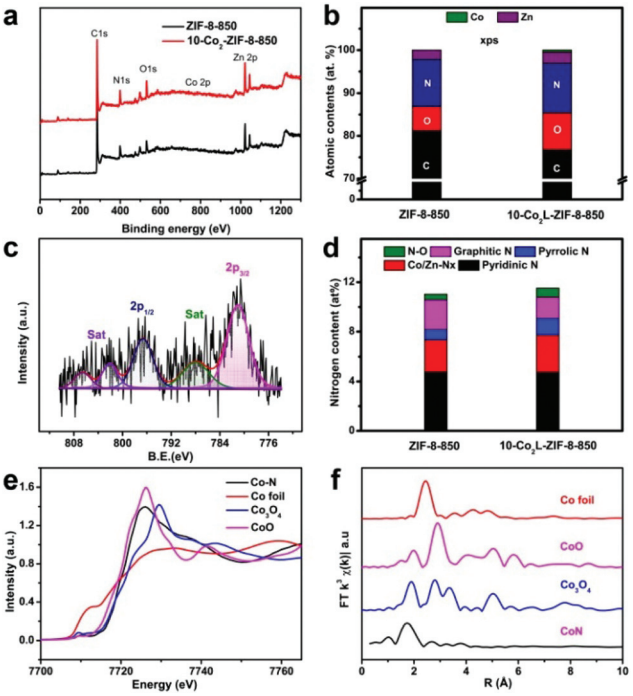


Fig. 3 (a) XPS spectra and (b) elemental composition of 10-$Co_2$L@ZIF-8-850 and ZIF-8-850, (c) high-resolution XPS spectrum of Co 2p in 10-$Co_2$L@ZIF-8-850, (d) atomic contents of the five different N species in 10-$Co_2$L@ZIF-8-850 and ZIF-8-850, (e) Co K-edge XANES profiles of 10-$Co_2$L@ZIF-8-850, $Co_3O_4$, CoO and Co foil and (f) Co K-edge $k^3$-weighted FT-EXAFS spectra of 10-$Co_2$L@ZIF-8-850, $Co_3O_4$, CoO and Co foil.

X-ray absorption near-edge spectroscopy (XANES) and extended X-ray absorption fine structure (EXAFS) analysis were carried out to further characterize the coordination environment and the electronic structure of 10-$Co_2$L@ZIF-8-850. As shown in Fig. 3e, the spectroscopic features of the Co K-edge in 10-$Co_2$L@ZIF-8-850 shifted towards the high energy relative to the Co foil. The oxidation state of Co in 10-$Co_2$L@ZIF-8-850 was close to +2, because the energy of the main absorption edge coincided with that of Co(2+)O. The peak at around 2.43 Å observed in the Fourier transform (FT) $k^3$-weighted EXAFS curve of Co foil (Fig. 3f) could be attributed to the Co–Co bond. The absence of the Co–Co bond confirmed the isolated dispersion of Co atoms in 10-$Co_2$L@ZIF-8-850. For CoO and $Co_3O_4$, the first major peak at ~1.92 Å could be assigned to the dominant Co–O coordination bonds. In contrast, the 10-$Co_2$L@ZIF-8-850 spectrum exhibited distinctive peak position at around 1.73 Å, which could be attributed to the Co–$N_xC_y$ bonds. The result was well consistent with the FT-EXAFS fitting one (Fig. S8 and Table S2†).

### 3.2. Electrocatalytic property

The electrocatalytic tests for the prepared catalysts were assessed by using an H-type cell in a standard three-electrode system. Linear sweep voltammograms (LSVs) were measured from 0 to −1.1 V *vs.* RHE (reversible hydrogen electrode; all

 This journal is © the Partner Organisations 2021

Published on 06 2021. Downloaded on 24.01.26 11:12:02.

potentials mentioned are *vs*. RHE hereafter) under Ar-bubbled and $CO_2$-bubbled 0.1 M $KHCO_3$ electrolyte, respectively. As shown in Fig. S9a,† the catalytic current density of 10-$Co_2$L@ZIF-8-850 under the $CO_2$ atmosphere increased slightly compared to that under Ar, indicating the strong competition reaction of the HER in aqueous electrolytes, and the syngas would be produced by the simultaneous reduction of $CO_2$ and $H_2O$. It should be noted that the electrocatalytic activity of *x*-$Co_2$L@ZIF-8-850 was closely related to the amount of $Co_2$L (*x*) in *x*-$Co_2$L@ZIF-8 composites. As shown in Fig. S9b,† ZIF-8-850 displays negligible electrocatalytic activity for $CO_2$ reduction, whereas *x*-$Co_2$L@ZIF-8-850 shows remarkably enhanced catalytic activity from −0.3 to −1.2 V, which underlines the crucial role of Co center in the activation of $CO_2$. Furthermore, with an increase in $Co_2$L, the catalytic performance of *x*-$Co_2$L@ZIF-8-850 evidently improved in terms of the onset potential, overpotential ($\eta$), and catalytic current, which further dominated the effect of Co amount on the catalytic activity. Among the tested *x*-$Co_2$L@ZIF-8-850, 10-$Co_2$L@ZIF-8-850 exhibited the best electrocatalytic activity. At −1.2 V, the current density of 10-$Co_2$L@ZIF-8-850 for syngas reached 46.3 mA $cm^{-2}$, about 7.7 times as high as that of ZIF-8-850 (Fig. S9b†). Gas chromatography (GC) and $^1$H NMR spectroscopy confirmed the presence of two gaseous products of CO and $H_2$ for all of the tested catalysts, and no liquid product was observed (Fig. S10†). Fig. 4a shows the current densities of CO ($j_{CO}$, red trace), $H_2$ ($j_{H_2}$, black trace), and the total current density under different potentials applied in a $CO_2$-saturated 0.1 M $KHCO_3$ (pH = 6.8) solution. It could be seen that at a certain potential, $j_{H_2}$ markedly increased than $j_{CO}$, which might be attributed to the low solubility and limited mass transfer for the $CO_2$ reduction reaction, whereas these factors would not influence the HER. At a potential of 1.0 V, the total current density of 10-$Co_2$L@ZIF-8-850 for $CO_2$ reduction and HER reached as high as 31.7 mA $cm^{-2}$. The value was significantly higher than those of the reported noble–metal or noble metal-free electrocatalysts (Table S2†).

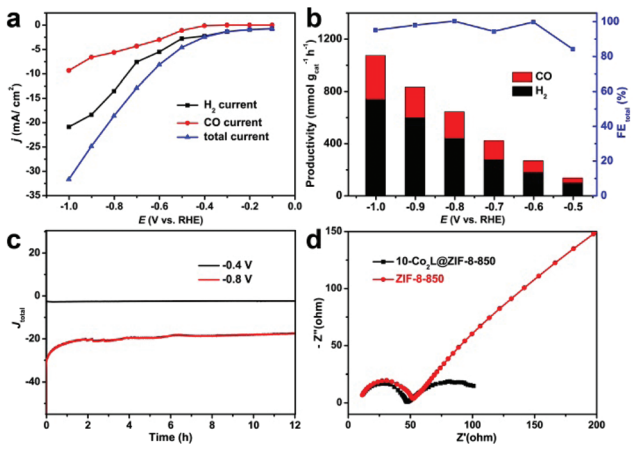


**Fig. 4** (a) LSV polarization curves of 10-$Co_2$L@ZIF-8-850 at 5 mV $s^{-1}$ in $CO_2$-saturated 0.1 M $KHCO_3$ solution (pH = 6.8). (b) The productivity (left *Y*-axis) and FE (right *Y*-axis) of 10-$Co_2$L@ZIF-8-850 under different applied potentials, where the red and dark columns represent CO and $H_2$, respectively. (c) Stability tests of 10-$Co_2$L@ZIF-8-850 at applied potentials of −0.4 and −0.8 V. (d) Nyquist plots of 10-$Co_2$L@ZIF-8-850 and ZIF-8-850.

The controlled potentiostatic electrolysis measurements of 10-$Co_2$L@ZIF-8-850 were further carried out under $CO_2$ atmosphere with potentials ranging from −0.5 to −1.0 V. The results showed that with a negative increase in the potentials, the productivity of syngas (CO + $H_2$) of 10-$Co_2$L@ZIF-8-850 increased substantially (Fig. 4b). At 1.0 V, the production yield reached as high as 1.08 mol $g^{-1}$ $h^{-1}$, significantly higher than that of ZIF-8-850 (0.071 mol $g^{-1}$ $h^{-1}$, Fig. S11†) and those of the most reported electrocatalysts.[37] It should be noted that during the broad electrochemical window (from −0.6 to −1.0 V), the total FE of CO and $H_2$ combined was over 96%, and the generated syngas ($CO/H_2$) exhibited a steady molar ratio of *ca.* 1 : 2. Evidently, the electrocatalytic performance of 10-$Co_2$L@ZIF-8-850 was better than those derived from $Co_2$L@ZIF-8-850 with 5, 20, and 40 mg $Co_2$L, respectively (Fig. S11†), as well as those from 10-$Co_2$L@ZIF-8 pyrolyzed at 750 and 950 °C, respectively (Fig. S12†). The relatively lower electrocatalytic performance could be attributed to the generation of $CoO_x$ nanoparticles during the preparation process. As shown in Fig. S13,† the diffraction peaks at 44.2° and 51.5° of 40-$Co_2$L@ZIF-8-850 can be indexed to Co NPs (PDF#15-0806), which confirm the formation of $CoO_x$ nanoparticles. In addition, we observed that the FE (CO + $H_2$) was lower than 100%. Besides the reason that small amounts of liquid products, such as formic acid and methanol, were generated (Fig. S14†), the reduction of $CoO_x$ might also be a non-negligible reason. In all, the above results demonstrate that the electrocatalytic performances of these catalysts were highly related to the precursor composition of the catalyst and the pyrolysis temperature.

The stability of 10-$Co_2$L@ZIF-8-850 was tested by long-term electrolysis at a constant potential of −0.4 and −0.8 V, respectively. As shown in Fig. 4c, after a continuous electrolysis for 10 h, a negligible degradation of current density was observed, which evidences that 10-$Co_2$L@ZIF-8-850 possesses good robustness. Evidently, the electrocatalytic features of 10-$Co_2$L@ZIF-8-850 discussed above will make it outstanding among the reported electrocatalysts for syngas production (Table S3†).

To reveal the excellent catalytic performance of 10-$Co_2$L@ZIF-8-850, the electrochemical impedance spectroscopy (EIS) measurements and electrochemically active surface areas (ECSAs) were investigated. The results showed that the diameter of the capacitive loop in the Nyquist plot of 10-$Co_2$L@ZIF-8-850 was smaller than those of *x*-$Co_2$L@ZIF-8-850 (*x* = 5, 20 and 40; Fig. S15a†) and 10-$Co_2$L@ZIF-8-T (T = 750 and 950 °C; Fig. S15b†), which indicated the smallest resistance for electron transfer in 10-$Co_2$L@ZIF-8-850 (Fig. 4d). As revealed by Raman spectroscopy, 10-$Co_2$L@ZIF-8-850 and ZIF-8-850 exhibited similar graphitic degrees; thus the conductivity was not a limiting factor for differentiating the electrocatalytic performance. ECSAs were then estimated from the

Published on 06 2021. Downloaded on 24.01.26 11:12:02.

electrochemical double-layer capacitance ($C_{dl}$). As shown in Fig. S16,† the 10-$Co_2$L@ZIF-8-850 electrode exhibits a larger $C_{dl}$ value (12.8 mF $cm^{-2}$) in contrast to ZIF-8-850 (10.6 mF $cm^{-2}$), indicating that 10-$Co_2$L@ZIF-8-850 possesses larger catalytic active surface areas. The higher ECSAs and rich active sites might significantly contribute to the high electrocatalytic efficiency of 10-$Co_2$L@ZIF-8-850 for syngas production.

## 4. Conclusions

In this study, we successfully fabricated a series of Co single-site C/$N_x$-based catalysts by a guest–host pyrolysis strategy, which could be used for the simultaneous electrocatalytic reduction of $CO_2$ and $H_2O$ to produce syngas with a tunable CO/$H_2$ molar ratio. This strategy proved to be facile, effective, and efficient. As expected, the as-prepared Co single-site catalyst exhibited a high efficiency for the electrocatalytic reduction of $CO_2$ and $H_2O$ to steadily produce syngas with a CO/$H_2$ molar ratio of 1 : 2. This work provides a new way for the preparation of carbon-based metal single-site electrocatalysts with high catalytic efficiencies.

## Conflicts of interest

There are no conflicts of interest to declare.

## Acknowledgements

This work was financially supported by the National Key R&D Program of China (2017YFA0700104), the National Natural Science Foundation of China (22071182, 21931007, 21861001, and 21790052), the 111 Project of China (D17003), and the Science and Technology Development Fund of Tianjin Education Commission for Higher Education (2018KJ129).

## References

1 A. Y. Khodakov, W. Chu and P. Fongarland, Advances in the Development of Novel Cobalt Fischer–Tropsch Catalysts forSynthesis of Long-Chain Hydrocarbons and Clean Fuels, *Chem. Rev.*, 2007, **107**, 1692–1744.
2 B. H. Zhao, Y. Huang, D. L. Liu, Y. F. Yu and B. Zhang, Integrating photocatalytic reduction of $CO_2$ with selective oxidation of tetrahydroisoquinoline over InP–$In_2O_3$ Z-scheme p-n junction, *Sci. China: Chem.*, 2019, **63**, 1–7.
3 S. Gao, Y. Lin, X. C. Jiao, Y. F. Sun, Q. Q. Luo, W. H. Zhang, D. Q. Li, J. L. Yang and Y. Xie, Partially oxidized atomic cobalt layers for carbon dioxide electroreduction to liquid fuel, *Nature*, 2016, **529**, 68–71.
4 J. W. Wang, W. J. Liu, D. C. Zhong and T. B. Lu, Nickel complexes as molecular catalysts for water splitting and $CO_2$ reduction, *Coord. Chem. Rev.*, 2019, **378**, 237–261.
5 D. C. Liu, D. C. Zhong and T. B. Lu, Non-noble metal-based molecular complexes for $CO_2$ reduction: From the ligand design perspective, *EnergyChem*, 2020, **2**, 100034.
6 Y. N. Yao, Y. Gao, L. Ye, H. Chen and L. Sun, Highly efficient photocatalytic reduction of $CO_2$ and $H_2O$ to CO and $H_2$ with a cobalt bipyridyl complex, *J. Energy Chem.*, 2018, **27**, 502–506.
7 T. T. Zheng, K. Jiang and H. T. Wang, Recent Advances in Electrochemical $CO_2$-to-CO Conversion on Heterogeneous Catalysts, *Adv. Mater.*, 2018, **30**, 1802066.
8 K. Yuan and Y. W. Zhang, Engineering well-defined rare earth oxide-based nanostructures for catalyzing $C_1$ chemical reactions, *Inorg. Chem. Front.*, 2020, **7**, 4256–4280.
9 D. F. Gao, H. Zhou, J. Wang, S. Miao, F. Yang, G. X. Wang, J. G. Wang and X. H. Bao, Size-Dependent Electrocatalytic Reduction of $CO_2$ over Pd Nanoparticles, *J. Am. Chem. Soc.*, 2015, **137**, 4288–4291.
10 H. S. Jeon, I. Sinev, F. Scholten, N. J. Divins, I. Zegkinoglou, L. Pielsticker and B. R. Cuenya, Operando Evolution of the Structure and Oxidation State of Size- Controlled Zn Nanoparticles during $CO_2$ Electroreduction, *J. Am. Chem. Soc.*, 2018, **140**, 9383–9386.
11 J. B. Zhang, R. G. Yin, Q. Shao, T. Zhu and X. Q. Huang, Oxygen Vacancies in Amorphous $InO_x$ Nanoribbons Enhance $CO_2$ Adsorption and Activation for $CO_2$ Electroreduction, *Angew. Chem., Int. Ed.*, 2019, **58**, 5609–5613.
12 S. B. Liu, J. Xiao, X. F. Lu, J. Wang, X. Wang and X. W. Lou, Efficient Electrochemical Reduction of $CO_2$ to HCOOH over Sub-2 nm $SnO_2$ Quantum Wires with Exposed Grain Boundaries, *Angew. Chem., Int. Ed.*, 2019, **58**, 8499–8503.
13 W. Y. Zhang, Q. Qin, D. Lei, R. X. Qin and N. F. Zheng, Electrochemical Reduction of $CO_2$ to $CH_3OH$ on hierarchical Pd/$SnO_2$ nanosheets with abundant Pd-O-Sn interfaces, *Angew. Chem., Int. Ed.*, 2018, **57**, 9475–9479.
14 R. He, X. Yuan, P. Shao, T. Duan and W. Zhu, Hybridization of Defective Tin Disulfide Nanosheets and Silver Nanowires Enables Efficient Electrochemical Reduction of $CO_2$ into Formate and Syngas, *Small*, 2019, **15**, 1904882.
15 S. J. Guo, S. Q. Zhao, X. Q. Wu, H. Li, Y. J. Zhou, C. Zhu, N. J. Yang, X. Jiang, J. Gao, L. Bai, Y. Liu, Y. Lifshitz, S. T. Lee and Z. H. Kang, A $Co_3O_4$-CDots-$C_3N_4$ three component electrocatalyst design concept for efficient and tunable $CO_2$ reduction to syngas, *Nat. Commun.*, 2017, **8**, 1828.
16 R. He, A. Zhang, Y. L. Ding, T. Y. Kong, Q. Xiao, H. L. Li, Y. Liu and J. Zeng, Achieving the Widest Range of Syngas Proportions at High Current Density over Cadmium Sulfoselenide Nanorods in $CO_2$ Electroreduction, *Adv. Mater.*, 2018, **30**, 1705872.
17 J. W. Wang, H. H. Huang, J. K. Sun, D. C. Zhong and T. B. Lu, Syngas Production with a Highly-Robust Nickel(II) Homogeneous Electrocatalyst in a Water-Containing System, *ACS Catal.*, 2018, **8**, 7612–7620.
18 S. R. Foit, I. C. Vinke, L. G. J. de Haart and R. A. Eichel, Power-to-Syngas: An Enabling Technology for the

 This journal is © the Partner Organisations 2021

Published on 06 2021. Downloaded on 24.01.26 11:12:02.

Transition of the Energy System?, *Angew. Chem., Int. Ed.*, 2017, **56**, 5402–5411.

19 L. A. Diaz, N. S. J. Gao, B. Adhikari, T. E. Lister, E. J. Dufek and A. D. Wilson, Electrochemical production of syngas from $CO_2$ captured in switchable polarity solvents, *Green Chem.*, 2018, **20**, 620–626.

20 B. H. Qin, Y. H. Li, H. Q. Fu, H. J. Wang, S. Z. Chen, Z. L. Liu and F. Peng, Electrochemical Reduction of $CO_2$ into Tunable Syngas Production by Regulating the Crystal Facets of Earth-Abundant Zn Catalyst, *ACS Appl. Mater. Interfaces*, 2018, **10**, 20530–20539.

21 W. C. Sheng, S. Kattel, S. Y. Yao, B. H. Yan, Z. X. Liang, C. J. Hawxhurst, Q. Y. Wu and J. G. G. Chen, Electrochemical reduction of $CO_2$ to synthesis gas with controlled $CO/H_2$ ratios, *Energy Environ. Sci.*, 2017, **10**, 1180–1185.

22 W. Xi, R. Z. Ma, H. Wang, Z. Gao, W. Q. Zhang and Y. F. Zhao, Ultrathin Ag Nanowires Electrode for Electrochemical Syngas Production from Carbon Dioxide, *ACS Sustainable Chem. Eng.*, 2018, **6**, 7687–7694.

23 M. B. Ross, C. T. Dinh, Y. Li, D. Kim, P. D. Luna, E. H. Sargent and P. D. Yang, Tunable Cu Enrichment Enables Designer Syngas Electrosynthesis from $CO_2$, *J. Am. Chem. Soc.*, 2017, **139**, 9359–9363.

24 X. Yuan, Y. Luo, B. Zhang, C. Dong, J. Lei, F. Yi, T. Duan, W. Zhu and R. He, Decoration of In nanoparticles on $In_2S_3$ nanosheets enables efficient electrochemical reduction of $CO_2$, *Chem. Commun.*, 2020, **56**, 4212–4215.

25 G. D. Li, S. L. Zhao, Y. Zhang and Z. Y. Tang, Metal–Organic Frameworks Encapsulating Active Nanoparticles as Emerging Composites for Catalysis: Recent Progress and Perspectives, *Adv. Mater.*, 2018, **30**, 1800702.

26 L. Y. Chen, R. Luque and Y. W. Li, Controllable design of tunable nanostructures inside metal–organic frameworks, *Chem. Soc. Rev.*, 2017, **46**, 4614–4630.

27 S. Mukhopadhyay, J. Debgupta, C. Singh, A. Kar and S. K. Das, A Keggin Polyoxometalate Shows Water Oxidation Activity at Neutral pH: POM@ZIF-8, an Efficient and Robust Electrocatalyst, *Angew. Chem., Int. Ed.*, 2018, **57**, 1918–1923.

28 Z. C. Kong, J. F. Liao, Y. J. Dong, Y. F. Xu, H. Y. Chen, D. B. Kuang and C. Y. Su, Core@Shell $CsPbBr_3$@Zeolitic Imidazolate Framework Nanocomposite for Efficient Photocatalytic $CO_2$ Reduction, *ACS Energy Lett.*, 2018, **3**, 2656–2662.

29 S. F. Ji, Y. J. Chen, S. Zhao, W. X. Chen, L. J. Shi, Y. Wang, J. C. Dong, Z. Li, F. W. Li, C. Chen, Q. Peng, J. Li, D. S. Wang and Y. D. Li, Atomically Dispersed Ruthenium Species Inside Metal-Organic Frameworks: Combining the High Activity of Atomic Sites and the Molecular Sieving Effect of MOFs, *Angew. Chem., Int. Ed.*, 2019, **58**, 4271–4275.

30 Y. T. Xu, X. F. Xiao, Z. M. Ye, S. L. Zhao, R. G. Shen, C. T. He, J. P. Zhang, Y. D. Li and X. M. Chen, Cage-Confinement Pyrolysis Route to Ultrasmall Tungsten Carbide Nanoparticles for Efficient Electrocatalytic Hydrogen Evolution, *J. Am. Chem. Soc.*, 2017, **139**, 5285–5288.

31 J. M. Chen, W. Wei, X. L. Feng and T. B. Lu, $CO_2$ fixation and transformation by a dinuclear copper cryptate under acidic conditions, *Chem. – Asian J.*, 2007, **2**, 710–719.

32 T. Ouyang, H. J. Wang, H. H. Huang, J. W. Wang, S. Guo, W. J. Liu, D. C. Zhong and T. B. Lu, Dinuclear Metal Synergistic Catalysis Boosts Photochemical $CO_2$-to-CO Conversion, *Angew. Chem., Int. Ed.*, 2018, **57**, 16480–16485.

33 T. Ouyang, H. H. Huang, J. W. Wang, D. C. Zhong and T. B. Lu, A Dinuclear Cobalt Cryptate as a Homogeneous Photocatalyst for Highly Selective and Efficient Visible-Light Driven $CO_2$ Reduction to CO in $CH_3CN/H_2O$ Solution, *Angew. Chem., Int. Ed.*, 2017, **129**, 756–761.

34 R. G. Ma, Y. Zhou, Y. F. Chen, P. X. Li, Q. Liu and J. C. Wang, Ultrafine Molybdenum Carbide Nanoparticles Composited with Carbon as a Highly Active Hydrogen-Evolution Electrocatalyst, *Angew. Chem., Int. Ed.*, 2015, **54**, 14723–14727.

35 C. M. Zhao, X. Y. Dai, T. Yao, W. X. Chen, X. Q. Wang, J. Wang, J. Yang, S. Q. Wei, Y. Wu and Y. D. Li, Ionic Exchange of Metal-Organic Frameworks to Access Single Nickel Sites for Efficient Electroreduction of $CO_2$, *J. Am. Chem. Soc.*, 2017, **139**, 8078–8081.

36 Q. P. Lin, X. H. Bu, A. G. Kong, C. Y. Mao, F. Bu and P. Y. Feng, Heterometal-Embedded Organic Conjugate Frameworks from Alternating Monomeric Iron and Cobalt Metalloporphyrins and Their Application in Design of Porous Carbon Catalysts, *Adv. Mater.*, 2015, **27**, 3431–3436.

37 X. Song, H. Zhang, Y. Yang, B. Zhang, M. Zuo, X. Cao, J. Sun, C. Lin, X. Li and Z. Jiang, Bifunctional Nitrogen and Cobalt Codoped Hollow Carbon for Electrochemical Syngas Production, *Adv. Sci.*, 2018, **5**, 1800177.